Mechanical Systems and Signal Processing 168 (2022) 108724

Contents lists available at ScienceDirect

Mechanical Systems and Signal Processing

journal homepage: www.elsevier.com/locate/ymssp

Dynamics and power limit analysis of a galloping piezoelectric energy harvester under forced excitation

Guobiao Hu [a,b], Chunbo Lan [c], Lihua Tang [d], Bo Zhou [b,e], Yaowen Yang [a,*]

[a] School of Civil and Environmental Engineering, Nanyang Technological University, Singapore
[b] State Key Laboratory of Structural Analysis for Industrial Equipment, Dalian University of Technology, China
[c] College of Aerospace Engineering, Nanjing University of Aeronautics and Astronautics, China
[d] Department of Mechanical Engineering, University of Auckland, New Zealand
[e] State Key Laboratory of Structural Analysis for Industrial Equipment, School of Naval Architecture Engineering, Dalian University of Technology, China

ARTICLE INFO

Keywords:
Piezoelectric energy harvesting
Galloping
Power limit
Impedance matching
Harmonic balance method
Multi-scale method
Equivalent circuit model

ABSTRACT

This paper presents a rigorous analytical solution to the dynamics of a single-degree-of-freedom (SDOF) piezoelectric energy harvester (PEH) under the combined wind and base excitations using the harmonic balance method. The boundaries of the quenching region are predicted using the multi-scale method. An equivalent circuit model (ECM) is established to verify the analytical solution, and the simulation results based on the ECM are in good agreement with the analytical ones. Subsequently, the power limit of the SDOF PEH under the combined excitations is analysed for the first time using the impedance theory based on a simplified model. The maximum power amplitudes at different excitation frequencies are also sought by numerically sweeping the load resistance. It is found that the impedance theory that has been successfully adopted in the literature is inapplicable in analysing the power limit of the SDOF PEH under the combined excitations. The impedance plots obtained based on resistance sweeping clearly indicate that, in contrast to the conclusions given in the literature, impedance matching is not the condition to attain the power limit of the SDOF PEH under the combined excitations. A mathematical proof is provided for a reasonable explanation. Finally, it is demonstrated that numerical simulations based on the original model can verify the power limit calculated based on the simplified model.

1. Introduction

In the past two decades, researchers have devoted enormous efforts to developing various vibration energy harvesters and the associated fundamental theories [1–6]. Due to the ubiquity of vibrations, vibration energy harvesting technology is deemed as a vital solution to enable low-power consumption Internet-of-Things (IoTs) devices to be self-sustained. Since the ambient vibration intensity is often small, most vibration energy harvesters are designed to operate near the resonance mode to achieve a considerable power output. However, the ambient vibration energy mostly spreads over a broad spectrum and features uncertainties [7,8]. Once the external excitation frequency even slightly deviates from the resonant frequency of an energy harvester, its performance could be drastically deteriorated. Wind induced by atmospheric motion is also one of the most ubiquitous nature sources on Earth. Based on flow-induced vibration phenomena, researchers have proposed various wind energy harvesting techniques. According to the physical

* Corresponding author.
E-mail address: cywyang@ntu.edu.sg (Y. Yang).

https://doi.org/10.1016/j.ymssp.2021.108724
Received 21 September 2021; Received in revised form 21 November 2021; Accepted 2 December 2021
Available online 22 December 2021

mechanisms behind flow-induced vibration phenomena, wind energy harvesters can be classified into vortex-induced vibration (VIV) [9,10], galloping [11–13], and flutter [14,15] energy harvesters. Galloping energy harvesters usually have low cut-in wind speeds and can operate over a wide range of wind speed. Therefore, galloping energy harvesting has received lots of research interest. Provided that the wind speed is sufficiently large, a properly designed galloping energy harvester is able to produce a considerable power output. As compared to vibration energy harvesters, galloping energy harvesting is exempted from the frequency dependency. From this perspective, galloping energy harvesting appears to be more promising.

In fact, there could be no significant difference between the design of an ordinary vibration energy harvester and a galloping energy harvester. By appropriately attaching a bluff body onto an ordinary vibration energy harvester, one can use it for galloping energy harvesting [16]. Similar to the development history of vibration energy harvesters, the design of galloping energy harvesters has evolved from linear [16–18] to nonlinear [19–22], and from single-degree-of-freedom (SDOF) [23] to multiple-degree-of-freedom (MDOF) [11,12,24,25]. Moreover, given the co-existence of winds and ambient vibrations in numerous scenarios, concurrent energy harvesting from the winds and base excitations has been proposed and investigated by researchers. Bibo *et al.* [26] studied a flutter energy harvester under the combined excitations of a base vibration and a wind load. They derived an approximate solution of the voltage response from the flutter energy harvester using the method of normal forms. They also conducted an experimental study for validation [27]. Dai *et al.* [28] considered a VIV-based piezoelectric energy harvester (PEH) under a base excitation and presented related simulation and experimental studies. However, analytical solutions to the VIV-based PEH under a base excitation were not provided. Through simulations and experiments, Yan *et al.* [29] and Bibo *et al.* [30] explored the dynamics of PEHs under the combined excitations of galloping and base vibration. Zhao *et al.* [21] introduced mechanical stoppers and magnetic bistable nonlinearity into a galloping energy harvester under base excitation. The experimental and simulation results indicated that the proposed concurrent energy harvester demonstrated a broadband ability. Analytical solutions to the mechanical and electrical responses of galloping PEHs could be found in the work by Yan *et al.* [31]. Zhao [32] further derived the analytical solution for an impact-engaged galloping PEH under a base excitation using the averaging method. The decoupling treatment adopted in [31,32] greatly simplified the mathematical problem. However, there lacks a solid proof behind that simplification. Therefore, one of the motivations of this work is to derive a more rigorous solution to the dynamic response of a galloping PEH under base excitation.

The aforementioned studies focused on analysing the mechanical dynamics of PEHs under the combined excitations of wind and base vibration. It is well-known that the circuit part also plays a significant role in affecting the performance of a PEH [33–38]. In the field of wind energy harvesting, Abdelmoula *et al.* [39] investigated the effect of electrical impedance on the performance of a galloping PEH. Zhao *et al.* [40] presented the analytical solutions to a galloping PEH shunted to the interface circuits, including synchronized switching harvesting on inductor (SSHI) and synchronized charge extraction (SCE). A later study was also conducted by Zhao *et al.* to compare the performance of four interface circuits for galloping energy harvesting [41]. In recent years, Liao *et al.* [42] proposed a concept of power limit to evaluate the overall performance of a PEH under base excitation. The power limit refers to the maximum power that can ever be attained from a given PEH. Liao *et al.* [43] then extended the study to investigate the power limit of a

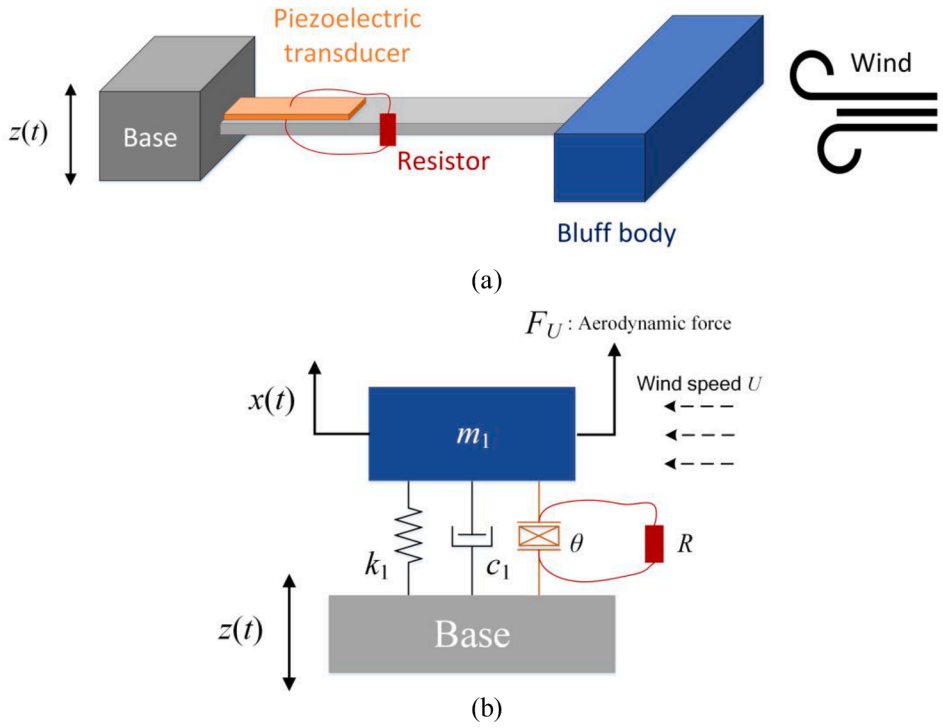

Fig. 1. (a) Schematic of a PEH under combined excitations of base vibration and aerodynamic force; (b) the corresponding SDOF model.

PEH shunted to an SSHI interface circuit. In more recent, Lan *et al.* [44] derived the power limit of a PEH with nonlinear stiffness. However, all the above studies are limited to the analyses of PEHs under base excitations. Studies on the power limit of a PEH under the combined wind and base excitations have yet been reported in the literature. Therefore, the other motivation of this paper is to present a first attempt to answer the question: what is the power limit of a PEH under the combined galloping and base excitations?

The rest of the paper is organized as follows. Section 2 overviews the SDOF PEH system to be investigated and gives the governing equations. In Section 3, an analytical solution to the dynamic response of the SDOF PEH under the combined excitations is derived. Section 4 presents a numerical verification of the derived analytical solution, along with a parametric study to reveal the effects of critical parameters on the energy harvesting performance of the SDOF PEH. The power limit of the SDOF PEH under the combined excitations is analysed in Section 5. The corresponding results and discussions are presented in Section 6. Finally, the concluding remarks are summarized in Section 7.

2. System overview and governing equations

Figure 1**(a)** shows the schematic of a PEH under combined excitations of base vibration and aerodynamic force. Without loss of generality, we can develop a lumped parameter model to describe the dynamics of the PEH. Since the response of the PEH around the fundamental resonance is of interest in this study, it can be simplified as an SDOF system as shown in Fig. 1**(b)**. The detailed procedures for deriving the lumped parameters of the SDOF PEH can be referred to [25]. The widely adopted SDOF modelling technique is directly employed hereinafter. The governing equations of the PEH can be written as:

$$m_1\ddot{x}(t)+c_1(\dot{x}(t)-\dot{z}(t))+k_1(x(t)-z(t))+\theta v(t)=\frac{1}{2}\rho LU^2d\left[s_1\frac{\dot{x}(t)}{U}-s_3\left(\frac{\dot{x}(t)}{U}\right)^3\right] \tag{1}$$

$$C_p\dot{v}(t)+\frac{v(t)}{R}=\theta(\dot{x}(t)-\dot{z}(t)) \tag{2}$$

where m_1, k_1, and c_1 are the mass, spring stiffness, and damping coefficient of the oscillator, respectively. θ is the electromechanical coupling coefficient of the attached piezoelectric transducer shunted with a resistor R. The clamped capacitance of the piezoelectric transducer is C_p. $x(t)$ and $z(t)$ are the displacements of the oscillator and the base, respectively. The wind of speed U applies an aerodynamic force F_U on the oscillator. ρ is the mass density of the air. s_1 and s_3 are the empirical linear and cubic coefficients of the transverse galloping force. The characteristic area of the bluff body normal to the wind flow is $L \times d$.

3. Analytical solution

This section presents the analytical solution to the dynamic responses of the SDOF PEH under the combined excitations.

3.1. Harmonic balance method

The harmonic balance method (HBM) is first adopted to seek the analytical solutions to the dynamic responses. The base displacement is assumed in the harmonic form as:

$$z(t)=Z_b sin(\omega_b t) \tag{3}$$

where Z_b is the displacement amplitude, and ω_b is the angular frequency. As the SDOF PEH is under the combined excitations of the base vibration and aerodynamic force, the displacement response of the SDOF PEH is assumed to contain two components.

$$x(t)=x_b(t)+x_g(t) \tag{4}$$

where $x_b(t)$ and $x_g(t)$ are the base excitation induced and the aerodynamic force induced response components, respectively. The subscripts b and g stand for base and galloping, respectively. To be specific, they are expressed as:

$$\begin{cases} x_b(t)=a_1(t)sin(\omega_b t)+b_1(t)cos(\omega_b t) \\ x_g(t)=g_1(t)sin(\omega_g t)+h_1(t)cos(\omega_g t) \end{cases} \tag{5}$$

Note that the self-excited response, i.e., $x_g(t)$, due to the galloping effect is also harmonic. From Eq. (2), it is learned that the voltage response is closely related to the displacement response. Thus, the voltage response is assumed in a similar form as:

$$v(t)=v_b(t)+v_g(t) \tag{6}$$

where the base excitation induced and the aerodynamic force induced components of the voltage response are concretely expressed as:

$$\begin{cases} v_b(t)=v_1(t)sin(\omega_b t)+v_2(t)cos(\omega_b t) \\ v_g(t)=v_3(t)sin(\omega_g t)+v_4(t)cos(\omega_g t) \end{cases} \tag{7}$$

Note from Eq. (2) that the displacement response $x(t)$ and the voltage response $v(t)$ are linearly coupled, thus we can derive the explicit relationship between $x(t)$ and $v(t)$, then represent $v(t)$ by $x(t)$. Substituting Eqs. (4) and into Eq. (6), then balancing the

harmonic components, we obtain the following four equations:

$$\begin{cases} -C_p v_2(t)\omega_b + \dfrac{v_1(t)}{R} + \theta b_1(t)\omega_b = 0 \\ C_p v_1(t)\omega_b + \dfrac{v_2(t)}{R} - \theta a_1(t)\omega_b + \theta Z_b \omega_b = 0 \\ -C_p v_4(t)\omega_g + \dfrac{c_1(t)}{R} + \theta h_1(t)\omega_g = 0 \\ C_p v_3(t)\omega_g + \dfrac{c_2(t)}{R} - \theta g_1(t)\omega_g = 0 \end{cases} \tag{8}$$

Solving Eq. (8), one can represent $v_1(t) \sim v_4(t)$ by $a_1(t) \sim h_1(t)$:

$$\begin{cases} v_1(t) = \dfrac{R\theta\omega_b\left(C_p a_1(t) R\omega_b - C_p R Z_b \omega_b - b_1(t)\right)}{C_p^2 R^2 \omega_b^2 + 1} \\ v_2(t) = \dfrac{R\theta\omega_b\left(C_p b_1(t) R\omega_b + a_1(t) - Z_b\right)}{C_p^2 R^2 \omega_b^2 + 1} \\ v_3(t) = \dfrac{R\theta\omega_g\left(C_p g_1(t) R\omega_g - h_1(t)\right)}{C_p^2 R^2 \omega_g^2 + 1} \\ v_4(t) = \dfrac{R\theta\omega_g\left(C_p h_1(t) R\omega_g + g_1(t)\right)}{C_p^2 R^2 \omega_g^2 + 1} \end{cases} \tag{9}$$

Substituting Eq. (9) into Eq. (6) and using the relationship in Eq. (5), one can express the voltage response $v(t)$ by $x_b(t)$ and $x_g(t)$ as

$$v(t) = \frac{K_{e1}}{\theta} x_b(t) - \frac{K_{e1}}{\theta} z_b(t) + \frac{K_{e2}}{\theta} x_g(t) + \frac{C_{e1}}{\theta\omega_b}\dot{x}_b(t) - \frac{C_{e1}}{\theta\omega_b}\dot{z}_b(t) - \frac{C_{e2}}{\theta\omega_g}\dot{x}_g(t) \tag{10}$$

where

$$\begin{cases} K_{e1} = \dfrac{R^2\theta^2\omega_b^2 C_p}{C_p^2 R^2 \omega_b^2 + 1} \quad K_{e2} = \dfrac{R^2\theta^2\omega_g^2 C_p}{C_p^2 R^2 \omega_g^2 + 1} \\ C_{e1} = \dfrac{R\theta^2\omega_b}{C_p^2 R^2 \omega_b^2 + 1} \quad C_{e2} = \dfrac{R\theta^2\omega_g}{C_p^2 R^2 \omega_g^2 + 1} \end{cases} \tag{11}$$

Substituting Eq. (10) into Eq. (1) eliminates the unknown variable $v(t)$. After eliminating $v(t)$, we substitute Eq. (5) into Eq. (1), then neglect the higher-order harmonics and balance the first-order harmonic terms. Four equations are obtained as follows:

$$\begin{aligned} &\left(-m_1\omega_b^2 + K_{e1} + k_1\right)a_1 + \left(-c_1\omega_b - C_{e1}\right)b_1 - K_{e1}Z_b - k_1 Z_b \\ &= \frac{1}{8U}\left(3Lr_1^2 d\rho s_3 \omega_b^3 + 6Lr_2^2 d\rho s_3 \omega_b \omega_g^2 - 4U^2\rho L d s_1 \omega_b\right)b_1 \end{aligned} \tag{12}$$

$$\begin{aligned} &\left(c_1\omega_b + C_{e1}\right)a_1 + \left(-m_1\omega_b^2 + K_{e1} + k_1\right)b_1 - \omega_b c_1 Z_b - C_{e1}Z_b \\ &= \frac{1}{8U}\left(-3Lr_1^2 d\rho s_3 \omega_b^3 - 6Lr_2^2 d\rho s_3 \omega_b \omega_g^2 + 4U^2\rho L d s_1 \omega_b\right)a_1 \end{aligned} \tag{13}$$

$$\begin{aligned} &\left(-m_1\omega_g^2 + K_{e2} + k_1\right)g_1 + \left(-c_1\omega_g - C_{e2}\right)h_1 \\ &= \frac{1}{8U}\left(6Lr_1^2 d\rho s_3 \omega_b^2 \omega_g + 3Lr_2^2 d\rho s_3 \omega_g^3 - 4LU^2 d\rho s_1 \omega_g\right)h_1 \end{aligned} \tag{14}$$

$$\begin{aligned} &\left(c_1\omega_g + C_{e2}\right)g_1 + \left(-m_1\omega_g^2 + K_{e2} + k_1\right)h_1 \\ &= \frac{1}{8U}\left(-6Lr_1^2 d\rho s_3 \omega_b^2 \omega_g - 3Lr_2^2 d\rho s_3 \omega_g^3 + 4LU^2 d\rho s_1 \omega_g\right)g_1 \end{aligned} \tag{15}$$

where

$$\begin{cases} r_1^2 = a_1^2 + b_1^2 \\ r_2^2 = g_1^2 + h_1^2 \end{cases} \tag{16}$$

It is worth noting that the time derivatives of the variables are forced to be zero to adapt to the steady-state assumption. The time

dependency is omitted at steady state, e.g., $a_1(t) \to a_1$. Multiplying Eq. (14) by $g_1(t)$, and Eq. (15) by $h_1(t)$, then adding up the two equations yields

$$-m_1\omega_g^2 + K_{e2} + k_1 = 0 \tag{17}$$

Solving Eq. (17) gives the solution of ω_g. On the other hand, by rearranging Eqs. (12)~ (15) and using Eq. (16) to simplify them, we obtain the following two equations:

$$\begin{aligned}
&-1024L^2U^4d^2r_1^2\rho^2s_1^2\omega_b^2 + 4096Ls_1\omega_b d\rho r_1^2(c_1\omega_b + C_{e1})U^3 \\
&+\left(1536L^2s_1s_3\omega_b^4d^2\rho^2r_1^4 + 4096\left(\omega_b^2c_1^2 + 2C_{e1}\omega_b c_1 + C_{e1}^2 + (K_{e1}+k_1)^2\right)Z_b^2\right)U^2 \\
&+\left(\begin{array}{l} -4096\omega_b^4m_1^2 - 8192C_{e1}\omega_b c_1 - 4096C_{e1}^2 - 4096(K_{e1}+k_1)^2 \\ +\left(3072L^2r_2^2s_1s_3\omega_g^2d^2\rho^2 - 4096c_1^2 + 8192m_1(K_{e1}+k_1)\right)\omega_b^2 \end{array}\right)r_1^2U^2 \\
&-6144\rho\left(r_2^2\omega_g^2 + \frac{\omega_b^2r_1^2}{2}\right)Ls_3\omega_b(c_1\omega_b + C_{e1})dr_1^2U \\
&-2304\rho^2\left(r_2^2\omega_g^2 + \frac{\omega_b^2r_1^2}{2}\right)^2L^2s_3^2\omega_b^2d^2r_1^2 = 0
\end{aligned} \tag{18}$$

$$\begin{aligned}
&\left(m_1^2\omega_g^4 + \left(-2K_{e2}m_1 + c_1^2 - 2k_1m_1\right)\omega_g^2 + 2c_1C_{e2}\omega_g + k_1^2 + 2K_{e2}k_1 + C_{e2}^2 + K_{e2}^2\right)r_2^2 \\
&\qquad = \frac{9L^2\left(2r_1^2s_3\omega_b^2 + r_2^2s_3\omega_g^2 - 4/3U^2s_1\right)^2d^2r_2^2\rho^2\omega_g^2}{64U^2}
\end{aligned} \tag{19}$$

Eqs. (18) and (19) only contain two unknown variables. Simultaneously solving them gives the solutions to r_1 and r_2. Substituting the solved r_1 and r_2 back into Eqs. (12) and (13), one obtains the corresponding a_1 and b_1. Finally, the voltage amplitudes of the base excitation induced and aerodynamic force induced components can be calculated as:

$$\begin{cases} V_b = \sqrt{\dfrac{K_{e1}}{C_p}\left(r_1^2 - 2a_1Z_b + Z_b^2\right)} \\ V_g = r_2\sqrt{\dfrac{K_{e2}}{C_p}} \end{cases} \tag{20}$$

In addition, the root-mean-square (RMS) voltage amplitude can be calculated as:

$$V_{RMS} = \sqrt{\frac{V_b^2 + V_g^2}{2}} \tag{21}$$

3.2. Multi-scale method

In addition to the harmonic balance method, the multi-scale method is also employed to provide insights into the dynamic characteristics of the SDOF PEH under the combined excitations. First, we define the fast and slow timescales $T_0 = t$ and $T_1 = \varepsilon t$, where ε is a booking parameter. The governing equation (i.e., Eq. (1)) of the SDOF PEH is written as:

$$\begin{aligned}
&m_1\ddot{x}(t) + \varepsilon c_1(\dot{x}(t) - \dot{z}(t)) + \omega_1^2m_1(x(t) - z(t)) + \varepsilon\theta v(t) \\
&\qquad = \frac{1}{2}\varepsilon\rho U^2Ld\left(s_1\frac{\dot{x}(t)}{U} - s_3\left(\frac{\dot{x}(t)}{U}\right)^3\right)
\end{aligned} \tag{22}$$

where $\omega_1 = \sqrt{k_1/m_1}$. According to the multi-scale method, the solutions are sought in the perturbed form as:

$$x(t) = x_0(T_0, T_1) + \varepsilon x_1(T_0, T_1) \tag{23}$$

$$v(t) = v_0(T_0, T_1) + \varepsilon v_1(T_0, T_1) \tag{24}$$

The time derivatives are thus changed to

$$\begin{aligned}
\frac{d}{dt} &= D_0 + \varepsilon D_1 + o\left(\varepsilon^2\right) \\
\frac{d^2}{dt^2} &= D_0^2 + 2\varepsilon D_0D_1 + o\left(\varepsilon^2\right)
\end{aligned} \tag{25}$$

where $D_0 = \partial/\partial T_0$ and $D_1 = \partial/\partial T_1$. Substituting Eqs. (23) and (24) into Eqs. (22) and (2), equating the coefficients of ε^0 on both sides of the equations gives:

$$D_{0,0}(x_0(T_0,T_1)) + \omega_1^2 x_0(T_0,T_1) = cos(\Omega T_0) Z_b \omega_1^2 \tag{26}$$

$$C_p D_1(v_0(T_0,T_1))R - D_1(x_0(T_0,T_1))R\theta + v_0(T_0,T_1) = sin(\Omega T_0)\Omega R Z_b \theta \tag{27}$$

where $D_{0,0} = \partial^2/\partial T_0^2$. Similarly, equating the coefficients of ε^1 on both sides of the equations gives:

$$\begin{aligned} &\omega_1^2 m_1 x_1(T_0,T_1) + 2m_1 D_{0,1}(x_0(T_0,T_1)) + m_1 D_{0,0}(x_1(T_0,T_1)) + D_0(x_0(T_0,T_1))c_1 \\ &+\theta v_0(T_0,T_1) = -\frac{1}{2U}\rho L d D_0(x_0(T_0,T_1))\left((D_0(x_0(T_0,T_1)))^2 s_3 - U^2 s_1\right) - sin(\Omega T_0)\Omega Z_b c_1 \end{aligned} \tag{28}$$

$$\begin{aligned} &C_p R D_1(v_0(T_0,T_1)) + C_p R D_0(v_1(T_0,T_1)) - \theta R D_1(x_0(T_0,T_1)) \\ &\qquad -\theta R D_0(x_1(T_0,T_1)) + v_1(T_0,T_1) = 0 \end{aligned} \tag{29}$$

where $D_{0,1} = \partial^2/\partial T_0 \partial T_1$. Eqs. (26) and (27) are first order linear differential equations, and the solutions can be easily obtained as:

$$\begin{cases} x_0(T_0,T_1) = A_1(T_1)e^{i\omega_1 T_0} + A_f e^{i\Omega T_0} + cc \\ v_0(T_0,T_1) = \dfrac{-i\omega_1\theta R A_1(T_1)e^{i\omega_1 T_0}}{1 + i\omega_1 R C_p} - \dfrac{i\Omega\theta R Z_b e^{i\Omega T_0}}{1 + i\Omega R C_p} - \dfrac{i\Omega\theta R A_f e^{i\Omega T_0}}{1 + i\Omega R C_p} + cc \end{cases} \tag{30}$$

where $A_f = \frac{\omega_1^2 Z_b}{-2\Omega^2 + 2\omega_1^2}$ and cc denotes the conjugate of the preceding terms. It is worth noting that the term $A_1(T_1)e^{i\omega_1 T_0}$ corresponds to the aerodynamic force induced response, and $A_f e^{i\Omega T_0}$ represents the base excitation induced response. Substituting Eq. (30) into Eq. (28), then eliminating the secular term yields:

$$\frac{d}{dT_1}A_1(T_1) = A_1(T_1)\left(\Gamma_{12} + i\Gamma_3 - \Gamma_4(|A_1(T_1)|)^2\right) \tag{31}$$

where $\Gamma_1 = \frac{\omega_1^2 C_p^2 (LUd\rho s_1 - 2c_1)R^2 + 2R\theta^2 + LUd\rho s_1 - 2c_1 - 2iC_p R^2\theta^2\omega_1}{4\left(C_p^2 R^2\omega_1^2 + 1\right)m_1}$, $\Gamma_2 = -\frac{3L\Omega^2 d\rho s_3}{2m_1 U}$, $\Gamma_{12} = \Gamma_1 - \Gamma_2 A_f^2$, $\Gamma_3 = -\frac{iC_p R^2\theta^2\omega_1}{2\left(C_p^2 R^2\omega_1^2 + 1\right)m_1}$, and $\Gamma_4 = -\frac{3Ld\rho s_3\omega_1^2}{4m_1 U}$.

Assuming the solution to Eq. (31) is in the form as:

$$A_1(T_1) = a_1(T_1)e^{i\theta_1(T_1)} \tag{32}$$

To simplify the calculation, the electromechanical coupling effect is assumed to ignorable. Thus, we intentionally let $C_p = 0$, $R = 0$, and $\theta = 0$. Subsequently, substituting Eq. (32) into Eq. (31), then separating the real and imaginary components yields:

$$\begin{cases} \dfrac{d}{dT_1}a_1(T_1) = \left(-(a_1(T_1))^2\Gamma_4 + \Gamma_{12}\right)a_1(T_1) \\ \dfrac{d}{dT_1}\theta_1(T_1) = 0 \end{cases} \tag{33}$$

Based on the first equation of Eq. (33), one can derive the solution to $a_1(T_1)$.

$$a_1(T_1) = \sqrt{\frac{\Gamma_{12}}{\Lambda\Gamma_{12}e^{-2\Gamma_{12}T_1} + \Gamma_4}} \tag{34}$$

where Λ is a constant of integration that is determined by the initial condition. It is noted that if $\Gamma_{12} > 0$, the denominator in the square root eventually approaches Γ_4, and $a_1(T_1)$ approaches $\sqrt{\Gamma_{12}/\Gamma_4}$. However, if $\Gamma_{12} < 0$, this denominator eventually approaches infinity, thus $a_1(T_1)$ approaches 0. Therefore, the solution to $\Gamma_{12} = 0$ offers a clue for predicting the existence of the aerodynamic force induced component.

$$\Gamma_{12} = \frac{6Ld\rho s_3\omega_1^4}{\Omega^2\left(-2\Omega^2 + 2\omega_1^2\right)^2} - LU^2 d\rho s_1 + 2Uc_1 = 0 \tag{35}$$

$a_1(T_1) = 0$ indicates that galloping disappears, which is the so-called quenching phenomenon [31]. Under the combined excitations, the quenching phenomenon occurs when the base excitation frequency approaches the resonant frequency of the PEH and the galloping is suppressed by the base excitation. Therefore, the solution to Eq. (35) predicts the boundaries of the quenching region.

4. Numerical verification and parametric study

In this section, an equivalent circuit model (ECM) is established to verify the above theoretical solutions. In fact, one can cast the governing equations into the state-space form, then use numerical methods such as the Runge-Kutta method, to obtain the numerical results. The equivalent circuit model is introduced not only for numerical verification, but also to familiarize the readers with the

equivalent circuit representation methodology, as it will be also adopted as a powerful tool to carry out the power limit analysis in the next section.

Figure 2 shows the ECM of SDOF PEH under the combined excitations. ECM is established based on the electrical–mechanical analogies. In brief, the force and velocity in the mechanical domain correspond to the voltage and current in the electrical domain. The mechanical elements, such as the mass, stiffness and damper, are equivalent to the inductor, capacitor and resistor, respectively. A nonlinear transfer function is used to represent the aerodynamic force. More detailed procedures for developing an ECM of a piezoelectric energy harvester can be referred to [9,12,45].

Figure 3**(a)** compares the analytical and numerical results of the RMS voltage amplitudes of the SDOF PEH under the combined excitations. The system parameters are listed in Table 1. The base excitation is controlled at a constant acceleration level of 1 m/s^2. From Fig. 3**(a)**, it can be seen that the analytical solutions derived in this study are in good agreement with the numerical results. The RMS voltage amplitude reaches the maximum near the resonant frequency of the SDOF PEH. Unlike the classic forced vibration of an SDOF PEH, after deviating from the resonant frequency, the RMS voltage amplitude first decreases, then 'abnormally' increases. Moreover, the RMS voltage amplitudes at the off-resonant frequencies are still considerably high. The voltage amplitudes of the base excitation induced and galloping induced components (V_b and V_g) presented in Fig. 3**(b)** provide the explanation for this phenomenon. It is observed that the voltage amplitude of the base excitation induced component, i.e., V_b, is just similar to a typical forced vibration frequency response. However, in addition to the base excitation induced voltage response, there also appears a galloping induced component due to the aerodynamic excitation. The galloping induced voltage response disappears near the resonant frequency of the SDOF PEH, while becomes significantly large when the SDOF PEH falls into an off-resonance state. It is thus revealed that the considerable voltage output from the SDOF PEH at the off-resonant frequencies is mainly originated from the galloping induced component, i.e., V_g. The grey-coloured area shown in Fig. 3**(b)** is the quenching region predicted by the multi-scale method (i.e., Eq. (35)). It represents the frequency range where the galloping induced component is suppressed by the base excitation. It can be found that the theoretical prediction matches well with the numerical result.

As mentioned in the introduction that Yan *et al.* [31] adopted a decoupling treatment for simplification and derived the analytical solutions to the same problem. Within the quenching region, where the galloping effect is suppressed, i.e., the galloping-induced component becomes zero, the decoupling treatment is coincidently valid. However, when the excitation frequency shifts away from the resonant frequency, and the quenching phenomenon disappears, a significant discrepancy may occur due to the decoupling treatment. To compare the methods developed in this study and [31], the analytical solutions derived using the method proposed in Yan *et al.* [31] are provided in Fig. 3. One can note in Fig. 3**(a)** that near the resonant frequency, the analytical solutions derived using the method proposed in Yan *et al.* [31] also match well with the numerical results. However, there exists unneglectable discrepancy at the off-resonance frequencies. In Fig. 3**(b)**, it can be clearly found that V_b predicted by both methods almost overlap with each other well. The discrepancy originates from the difference between their predictions about V_g. Considering the analytical solutions derived in this study are in good agreement with the numerical results, the analytical solutions derived using the method proposed in Yan *et al.* [31] overestimate V_g before the resonant peak and underestimate V_g after the resonant peak. The comparison results basically agree with the verification results presented in Yan *et al.* [31].

To provide more insights into the dynamic characteristics of the SDOF PEH, the time-domain responses at three typical frequencies (marked in Fig. 3**(b)** as Cases A, B, and C) are examined. For Case A, the base excitation frequency is set to be $f/f_1 = 0.85$. According to the theoretical prediction, the voltage amplitudes of the base excitation induced and galloping induced components are, respectively, $V_b = 7.07$ V and $V_g = 33.21$ V. Fig. 4**(a)** shows the time-history voltage response of the SDOF PEH obtained from the numerical simulation. Fig. 4**(b)** shows an enlarged view of the steady-state voltage response. It is directly observed that the response resembles a modulated signal which contains more than one frequency component. Fig. 4**(c)** presents the fast Fourier transform (FFT) amplitude of the steady-state voltage response in Fig. 4**(b)**. The FFT result clearly indicates that the voltage response contains two frequency components. The amplitudes of the two components are 7.067 V and 32.57 V, which agree well with the theoretical prediction. Moreover, the corresponding frequencies of the two components are 3.06 Hz and 3.606 Hz, respectively. By a simple calculation, one can find that 3.606 Hz $\approx f_1 = \sqrt{k_1/m_1}/2\pi$, and 3.06 Hz $\approx 0.85 f_1$.

For Case B, the base excitation frequency is tuned to the resonant frequency of the SDOF PEH, i.e., $f/f_1 = 1$. The theoretical analysis predicts that the galloping induced voltage response is supposed to disappear ($V_g = 0$ V), and the base excitation induced voltage amplitude, i.e., V_b, is about 66.65 V. Fig. 5 shows the simulated time-history voltage response, the steady-state voltage response, and the corresponding FFT amplitude of the SDOF PEH. It can be easily identified from the numerical results that the voltage response is

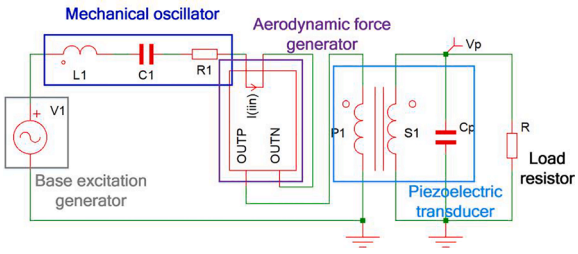

Fig. 2. Equivalent circuit model of SDOF PEH under combined excitations.

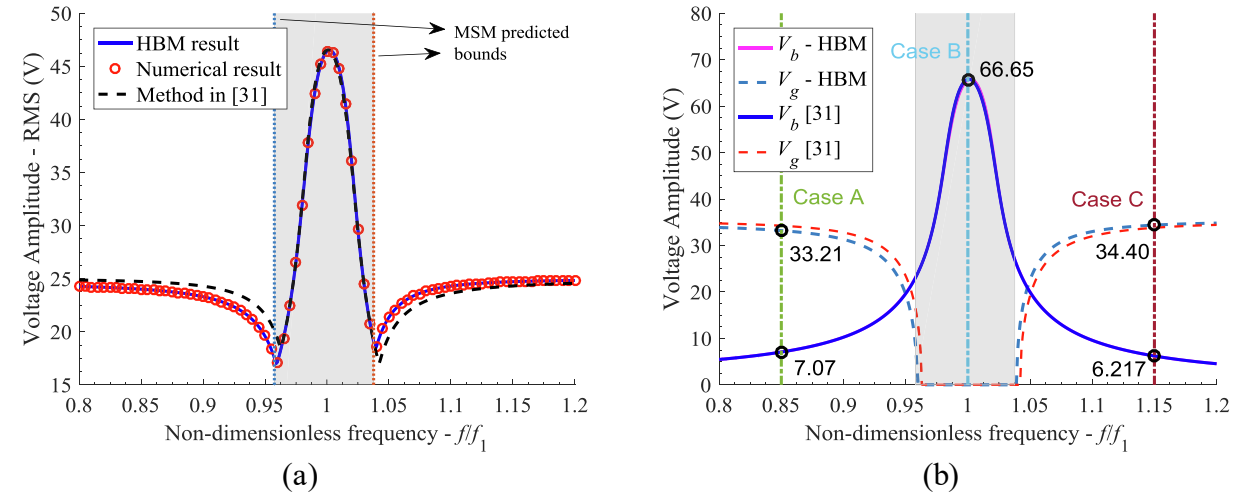

Fig. 3. (a) Comparison of harmonic balance method (HBM) predicted results and numerical results of RMS voltage amplitude; (b) HBM predicted voltage amplitudes of base excitation induced and galloping induced components. The grey-coloured area is the quenching region, i.e., the frequency range within which $V_g = 0$, predicted by the multi-scale method (MSM) (i.e., Eq. (35)).

Table 1
System parameters of SDOF PEH under investigation.

Electro-Mechanical parameters			
Effective mass m1 (g)	113.4	Electromechanical coupling θ (μN/V)	190
Effective stiffness k_1 (N/m)	58.02	Capacitance C_p (nF)	187
Damping ratio ζ_1	0.003	Load resistance R (Ω)	10^{12}
Aerodynamic parameters			
Air Density, ρ (kg/m^3)	1.24	Bluff body height, L (m)	0.1
Cross flow dimension, D_B (m)	0.05	Linear aerodynamic coefficient, s_1	2.5
Cubic aerodynamic coefficient, s_3	130	Wind speed U (m/s)	6

harmonic, and the FFT spectrum plot is clean with only a single sharp peak. The frequency and the amplitude of the sole component are 3.6 Hz $\approx f_1$ and 65.7 V, respectively. The numerical results agree with the theoretical predictions well.

In the last Case C, the base excitation frequency is further increased to be larger than the resonant frequency of the SDOF PEH, i.e., $f/f_1 = 1.15$. It is predicted by the theoretical analysis that the base excitation drives the SDOF PEH to vibrate, and the voltage amplitude produced due to the base excitation is about 6.217 V. In addition, the aerodynamic force activates the galloping oscillation of the SDOF PEH to produce a voltage output of 34.4 V. Fig. 6 presents the corresponding time-history response and FFT spectrum obtained from the numerical simulation. The numerical results confirm the appearance of the galloping induced voltage component. Moreover, the amplitudes of both components identified from the numerical results are $V_b = 6.187$ V and $V_g = 33.27$ V. Again, a good agreement is noted as compared to the theoretical prediction.

The verified analytical solution provides a computationally much faster means for system performance prediction as compared to the numerical simulation. Therefore, a parametric study is then performed based on the analytical solution to investigate the effects of system parameters on the dynamics and energy harvesting performance of the SDOF PEH. Fig. 7**(a) and (b)** reveal the voltage amplitude profile for varying wind speed and base excitation frequency. The other parameters are kept the same as listed in Table 1. It can be noted in Fig. 7**(a)** that in general, the RMS voltage increases with the wind speed. Moreover, the RMS voltage produced by the SDOF PEH at the off-resonant frequencies becomes comparably large with the increase of wind speed. From Fig. 7**(b)**, we can clearly compare and distinguish the contributions from the base excitation induced and galloping induced components. It is noted that when the wind speed is low, the galloping induced component disappears, i.e., the galloping phenomenon is inactivated. With the increase of the wind speed, the galloping phenomenon is activated and becomes more evident, leading to an increased V_g. Moreover, it is noted that increasing the wind speed does not only improve the galloping induced voltage amplitude V_g, but also results in an increase in the base excitation induced voltage amplitude V_b, especially around the resonant frequency of the SDOF PEH, i.e., $f/f_1 = 1$. This is because the aerodynamic force brings a negative damping effect on the SDOF PEH. With the increase of the wind speed, the total effective damping coefficient of the SDOF PEH becomes smaller, thus the base excitation induced response (e.g., displacement and voltage) becomes larger.

Figure 7**(c) and (d)** display the voltage amplitudes of the SDOF PEH versus the non-dimensional electromechanical coupling strength, i.e., $\alpha = \theta/(190\ \mu N/V)$, and the base excitation frequency. Putting aside the effect of the base excitation frequency, which has been discussed above, it is noted in Fig. 7**(c)** that the resonant peak is bent toward higher frequency with the increase of the wind

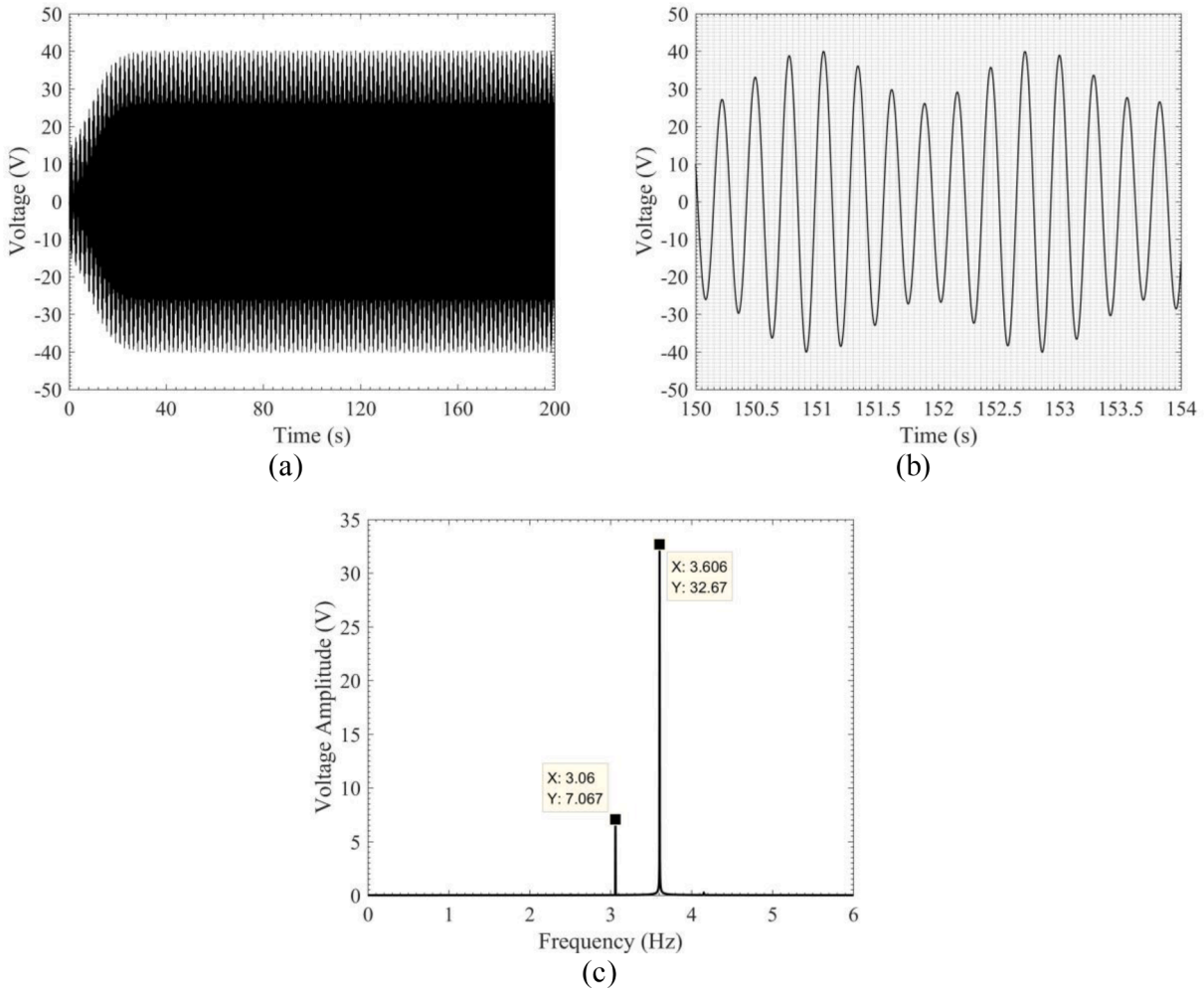

Fig. 4. (a) Time-history voltage response of SDOF PEH under base excitation with frequency of $f/f_1 = 0.85$; (b) enlarged view of steady-state voltage response over the time period from 150 s to 154 s; (c) fast Fourier transform (FFT) amplitude of steady-state voltage response.

speed. Fig. 7**(d)** further shows that both the base excitation induced and galloping induced voltage response components exhibit a similar bending phenomenon. This phenomenon is easily understandable by referring to the electromechanical coupling mechanism that the electrical domain also affects the dynamics of the mechanical domain. With the increase of the electromechanical coupling strength, the electrical domain brings a significant change in the total effective stiffness of the SDOF PEH, resulting in the shift of the resonant peak. It is clear in Fig. 7**(c) and (d)** that a stronger electromechanical coupling is associated with a larger total effective stiffness or a higher resonant frequency.

5. Power limit analysis

In the previous sections, analytical solutions to the SDOF PEH and the effects of various parameters on its energy harvesting performance have been presented and investigated. This section aims to analyse the power limit of the SDOF PEH. As well-known and has been partially revealed in Fig. 7**(c)**, the energy output from a PEH increases with the electromechanical coupling strength. However, once the electromechanical coupling strength reaches a certain high level, the power output saturates, i.e., it cannot be further increased. The power saturation phenomenon indicates an overall maximum power that can be attained for a given PEH. The overall maximum power that is attainable is termed the power limit. Obviously, a PEH with a higher power limit represents a better design under given constraints of material and structural strength. Therefore, we can use the power limit as a figure of merit to evaluate the design of a PEH. As mentioned in the introductory section, studies have been conducted to investigate the power limit of conventional base-excited PEH [42,44]. Yet, related study to examine the power limit of a PEH under the combined excitations has not been reported. The difficulties in the analysis of a PEH under the combined excitations have been briefly mentioned in the introduction. The details of the challenge will be elaborated in this section.

The impedance method has been proven to be powerful in investigating the power limit of a PEH [42,44]. However, it is only

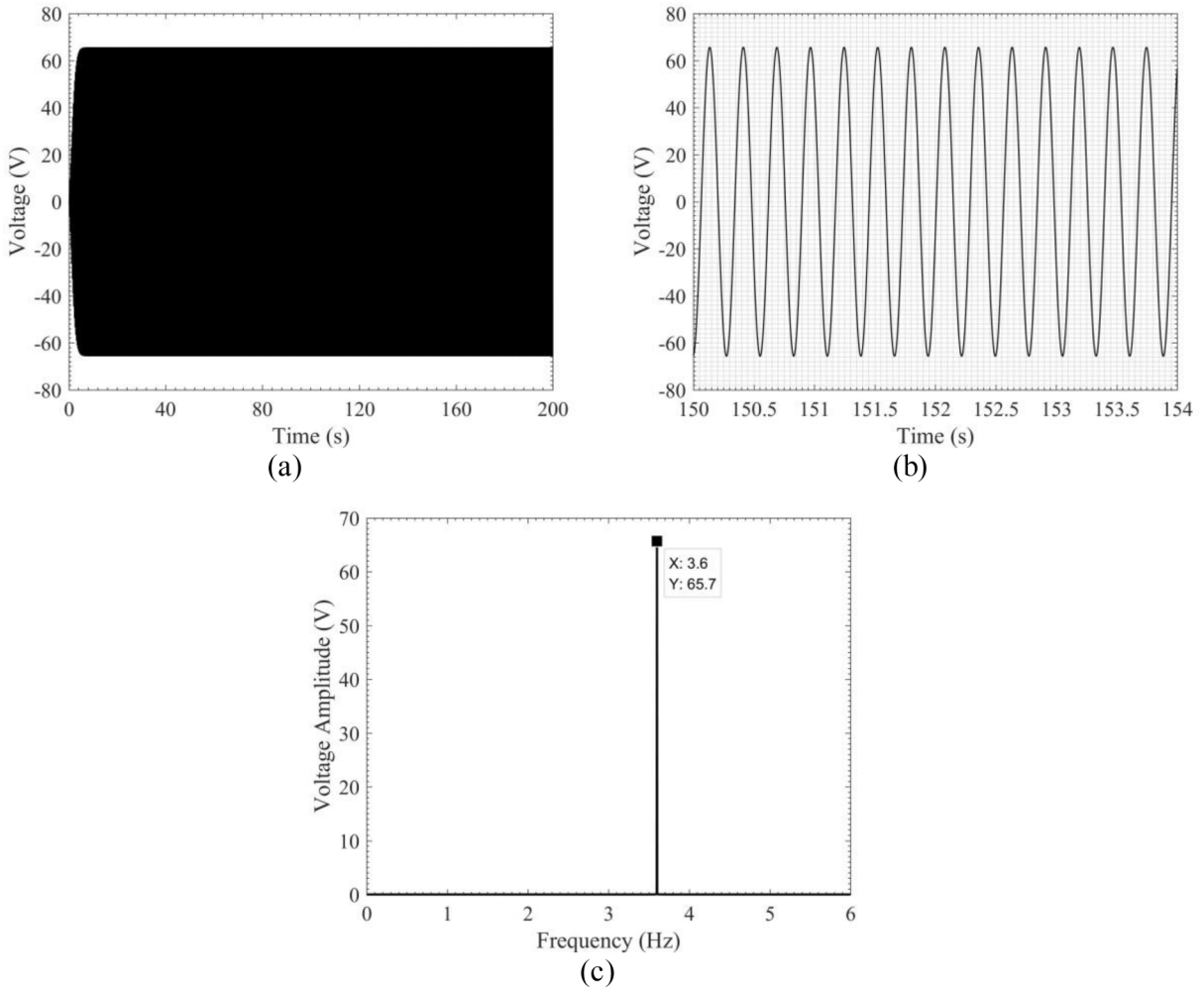

Fig. 5. (a) Time-history voltage response of SDOF PEH under base excitation with frequency of $f/f_1 = 1$; (b) enlarged view of steady-state voltage response over the time period from 150 s to 154 s; (c) fast Fourier transform (FFT) amplitude of steady-state voltage response.

applicable for linear systems. For a galloping PEH, the aerodynamic force in the governing equations brings nonlinearity. Therefore, the following treatments are implemented to simplify the problem. The numerical examples at the end of this section will justify the simplifications.

First, the governing equation is rewritten in the form as:

$$\begin{aligned} &m_1\ddot{y}(t) + c_1\dot{y}(t) + k_1 y(t) + \theta v(t) \\ &= \frac{1}{2}\rho L U^2 d\left[s_1\frac{\dot{y}(t)}{U} - s_3\left(\frac{\dot{y}(t)}{U}\right)^3\right] - m_1\ddot{z}(t) \end{aligned} \tag{36}$$

where $y(t)$ is the relative displacement of the SDOF PEH to the base, i.e., $y(t) = x(t)$-$z(t)$. In fact, the third-order term at the right hand side of Eq. (36) should be $\left(\frac{\dot{y}(t)+\dot{z}(t)}{U}\right)^3$. The primary reason that we can intentionally omit $\dot{z}(t)$ is given as follows. Considering that the power limit happens only near the resonance state of the SDOF PEH, the velocity of the SDOF PEH, i.e., $\dot{y}(t)$, at the resonance state is much larger than $\dot{z}(t)$. Thus, it is inferred that neglecting $\dot{z}(t)$ will not result in a remarkable error but will significantly ease the analysis.

Subsequently, the governing equations are recast in the following form:

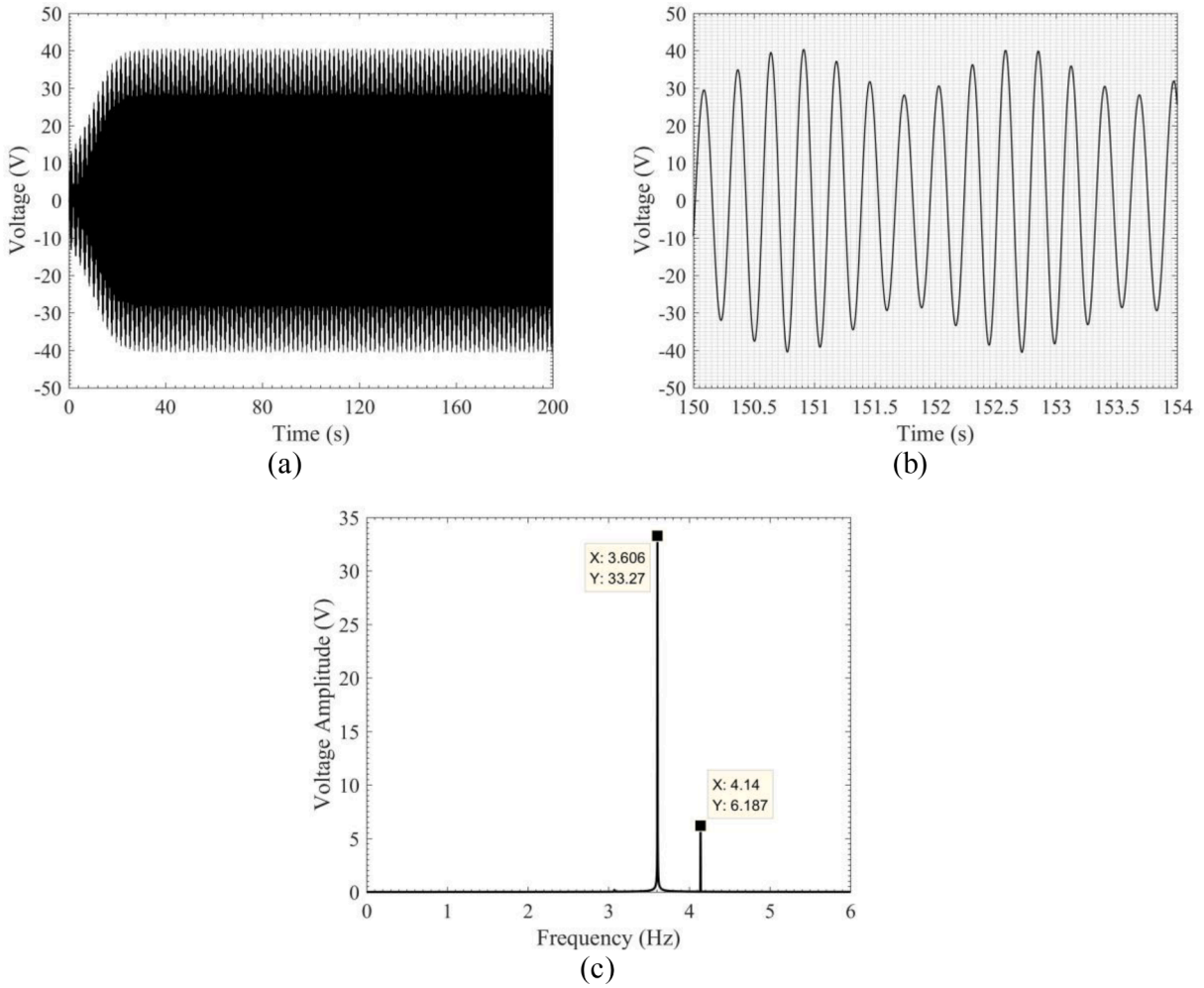

Fig. 6. (a) Time-history voltage response of SDOF PEH under base excitation with frequency of $f/f_1 = 1$; (b) enlarged view of the steady-state voltage response over the time period from 150 s to 154 s; (c) fast Fourier transform (FFT) amplitude of steady-state voltage response.

$$\frac{m_1}{\theta^2}\frac{d}{dt}[-\theta\dot{y}(t)] + \frac{c_1}{\theta^2}[-\theta\dot{y}(t)] + \frac{k_1}{\theta^2}\int[-\theta\dot{y}(t)]dt + \theta v(t) = \frac{\rho L U^2 d}{2\theta^2}\left[s_1\frac{\theta\dot{y}(t)}{U} - s_3\left(\frac{\theta\dot{y}(t)}{U}\right)^3\right] - \frac{m_1}{\theta}\ddot{z}(t) \tag{37}$$

$$C_p\dot{v}(t) + \frac{v(t)}{R} = \theta\dot{y}(t) \tag{38}$$

By comparing Eqs. (37) and (38) with typical differential equations of electrical circuits, we find that they have exactly the same mathematical form. Thus, we can establish an equivalent circuit model (ECM) that abides by the same governing equations. The equivalent elements of the circuit model are:

$$L_s = \frac{m_1}{\theta^2}, \quad C_s = \frac{\theta^2}{k_1}, \quad R_s = \frac{c_1}{\theta^2}, \quad V_{eq} = -\frac{m_1 A_{cc}}{\theta}, \quad i_{eq} = -\theta\dot{y}(t) \tag{39}$$

For the nonlinear aerodynamic force, using the harmonic balance method and neglecting the higher-order harmonics, we can linearize it as:

$$\frac{\rho L U^2 d}{2\theta^2}\left[s_1\frac{\theta\dot{y}(t)}{U} - s_3\left(\frac{\theta\dot{y}(t)}{U}\right)^3\right] \approx \left[\frac{s_1\rho L U d}{2\theta^2} - \frac{3s_3\rho L d}{8U\theta^2}\omega^2 r^2\right]\theta\dot{y}(t) \tag{40}$$

where r is the amplitude of $y(t)$. The detailed derivation and proof can be referred to [44]. Based on Eq., (40) we can represent the

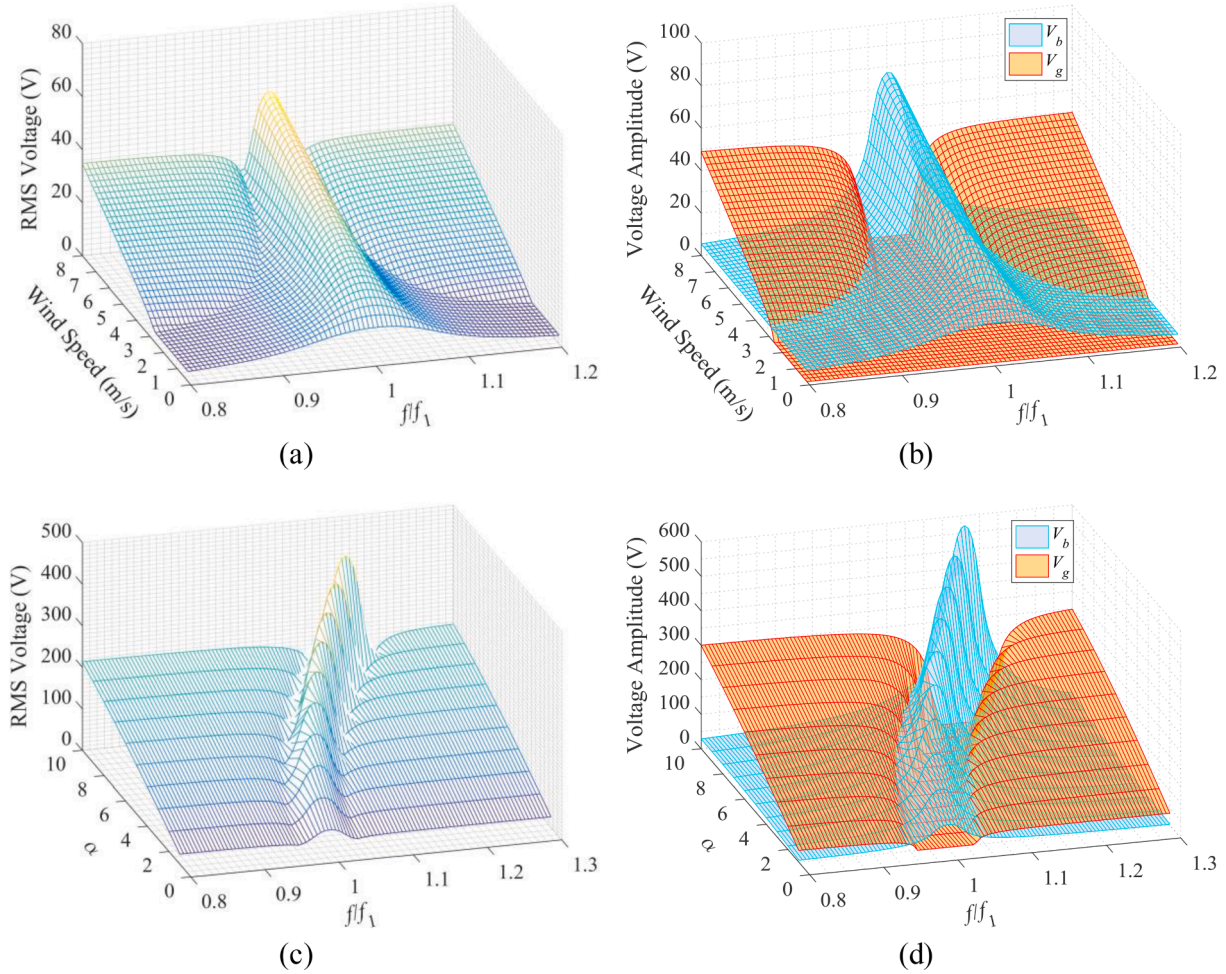

Fig. 7. (a) Analytical predictions of RMS voltage and (b) voltage amplitudes V_b & V_g versus wind speed (U) and dimensionless excitation frequency (f/f_1); (c) analytical predictions of RMS voltage and (d) voltage amplitudes V_b & V_g versus dimensionless electromechanical coupling coefficient (α) and dimensionless excitation frequency (f/f_1).

aerodynamic force term as a variable resistor in the equivalent circuit. The nonlinear resistor is frequency-dependent and amplitude-dependent as follows

$$R_n = \frac{1}{\theta^2}\left(-\frac{s_1\rho LUd}{2} + \frac{3s_3\rho Ld}{8U}\omega^2 r^2\right) \tag{41}$$

Figure 8 shows the schematic of the obtained ECM. Note the difference from the ECM presented in Fig. 2 that the aerodynamic force term is linearized and represented by a variable resistor rather than a nonlinear transfer function.

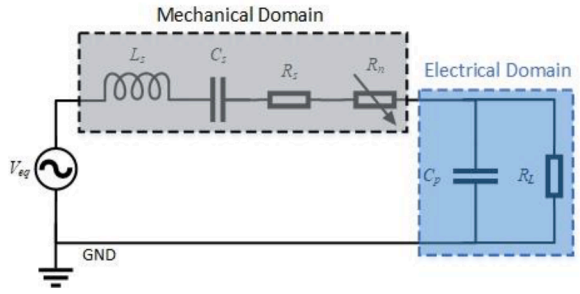

Fig. 8. Equivalent circuit representation of SDOF PEH under combined excitations.

In Fig. 8, it is noted that the equivalent electrical elements of the mechanical domain can be deemed as the internal impedance of the voltage source. The internal impedance can be written as:

$$Z_{mech} = i\omega L_s + R_s + R_n + \frac{1}{i\omega C_s} \tag{42}$$

The load resistor together R_L with the piezoelectric capacitance C_p constitute the external load impedance.

$$Z_{elec} = \frac{1}{i\omega C_p} || Z_L \tag{43}$$

where $Z_L = R_L + iX_L$. We temporarily assume the electrical load has an imaginary part X_L, i.e., reactance. According to the studies in [42,44], the power limit can be attained when the external impedance matches the internal impedance. In other words, the external impedance expressed in the complex number form must equal the complex conjugate of the internal impedance. As a result, the reactance components cancel each other, and the power limit will only depend on the resistance component of the internal impedance. The impedance matching theory requires:

$$Z_{elec} = Z^*_{mech} \tag{44}$$

where the asterisk subscript indicates taking the conjugate of the parameter. Substituting Eqs. (42) and (43) into Eq. (44) yields the optimal load that can satisfy the impedance matching condition.

$$\begin{cases} R_L = \dfrac{(c_1 - c_{n1} + c_{n3})\theta^2}{\left(\theta^2 + C_p\left(k_1 - m_1\omega^2\right)\right)^2 + (c_1 - c_{n1} + c_{n3})^2\omega^2 C_p^2} \\ X_L = \dfrac{\left(-m_1\omega^2 + k_1\right)\left[\theta^2 + C_p\left(k_1 - m_1\omega^2\right)\right] + (c_1 - c_{n1} + c_{n3})^2\omega^2 C_p}{\omega\left[\left(\theta^2 + C_p\left(k_1 - m_1\omega^2\right)\right)^2 + (c_1 - c_{n1} + c_{n3})^2\omega^2 C_p^2\right]} \end{cases} \tag{45}$$

where $c_{n1} = \frac{s_1\rho LUd}{2}$, and $c_{n3} = \frac{3s_3\rho Ld}{8U}\omega^2 r^2$. For the condition on R_L in Eq. (45), we know it is easily achievable regardless of the electromechanical coupling strength, since we can always select a suitable resistor with the desired value. Whether the condition on X_L can be satisfied determines whether impedance matching can be realized. Recalling that the study presented in this paper is limited on the SDOF PEH shunted to a resistive load, X_L needs to be zero to attain the power limit. Once the system parameters are given, the problem becomes: by only varying the excitation frequency ω, can X_L be tuned to zero? To answer this question, we force the numerator of X_L to be zero.

$$\left(-m_1\omega^2 + k_1\right)\left[\theta^2 + C_p\left(k_1 - m_1\omega^2\right)\right] + (c_1 - c_{n1} + c_{n3})^2\omega^2 C_p = 0 \tag{46}$$

By rearranging Eq. (46), one will notice that it is actually a quadratic equation of ω^2. Since the nature of ω requires it to be a real positive number, the solution to Eq. (46) must be a real positive number as well. Using the Vieta's formulas, we can easily obtain the explicit expressions of the solutions to Eq. (46). A necessary condition to ensure that Eq. (46) has real solutions is found to be:

$$\Delta = \left[(c_1 - c_{n1} + c_{n3})^2 C_p - m_1\theta^2\right]^2 - 4k_1 m_1 C_p^2 (c_1 - c_{n1} + c_{n3})^2 > 0 \tag{47}$$

Rearranging Eq. (47) yields:

$$\Theta^2 > 4\zeta_1\left(1 - \frac{c_{n1}}{c_1} + \frac{c_{n3}}{c_1}\right) + 4\zeta_1^2\left(1 - \frac{c_{n1}}{c_1} + \frac{c_{n3}}{c_1}\right)^2 \tag{48}$$

where $\Theta^2 = \frac{\theta^2}{C_p k_1}$ is a non-dimensional parameter that indicates the electromechanical coupling strength, and $\zeta_1 = \frac{c_1}{2\sqrt{k_1 m_1}}$. Eq. (48) manifests that only when the coupling strength, i.e., Θ^2, is sufficiently large, the impedance matching condition becomes attainable. Moreover, when Eq. (48) is valid, there should exist two solutions. When $\Delta = 0$, i.e., the sign of GT (greater than) in Eq. (48) becomes the sign of equality, there exists only a single solution. By convention, we refer to the situations of two solutions, a single solution and no solution, respectively, as the strongly coupled, critically coupled and weakly coupled cases. Under the assumption of impedance matching, the power limit can be obtained:

$$P_{lim} = \frac{V_{eq}^2}{4(R_s + R_n)} = \frac{(m_1 A_{cc})^2}{4\left(c_1 - \frac{s_1\rho LUd}{2} + \frac{3s_3\rho Ld}{8U}\omega^2 r^2\right)} \tag{49}$$

Unlike the linear PEH investigated in [42] and the nonlinear PEH studied in [44], the internal resistance, i.e., the denominator of Eq. (49), of the SDOF PEH under the combined excitations is not a constant, but a frequency and amplitude-dependent variable. That is to say, we still cannot ascertain the power limit based on the current form of Eq. (49). To obtain the power limit, the corresponding ω an r in Eq. (49) must be determined first. On one hand, turning back to the harmonic balance method derived solution in Section 3.1 will complicate the problem. On the other hand, the governing equations have actually been simplified at the most beginning of the power limit analysis. Therefore, a simpler approach is proposed to seek the solution to the unknown variables ω an r in Eq. (49).

Applying the Laplace transform to Eqs. (36) and (38), then eliminating the unknown parameter, one obtains an equation of r, as well as ω.

$$F_1 = r^2\left[\left(-\omega^2 m_1 + k_1 + k_e\right)^2 + \omega^2(c_1 - c_{n1} + c_{n3} + c_e)^2\right] - (m_1 A_{cc})^2 = 0 \tag{50}$$

where $k_e = \frac{C_p(\theta R_L\omega)^2}{1+(C_p R_L\omega)^2}$, and $c_e = \frac{R_L\theta^2}{1+(C_p R_L\omega)^2}$. R_L needs to be replaced by the matched resistance in Eq. (45), which is in turn a function of ω and r. It is worth mentioning that Eq. (50) is only applicable around the resonance state of the SDOF PEH, since the prerequisite for obtaining Eq. (50) is that the galloping induced component disappears. Recalling that the impedance matching condition requires X_L to be zero, another equation is then obtained:

$$F_2 = \left(-m_1\omega^2 + k_1\right)\left[\theta^2 + C_p\left(k_1 - m_1\omega^2\right)\right] + (c_1 - c_{n1} + c_{n3})^2\omega^2 C_p = 0 \tag{51}$$

Solving Eqs. (50) and (51) gives the solution to ω and r. Substituting them back into Eq. (49) yields the power limit.

6. Results and discussions

For the given system parameters listed in Table 1, the power limit of the SDOF PEH is computed using the method developed in Section 5. Due to the complexities of Eqs. (50) and (51), a graphical approach is adopted to seek the solutions. Briefly speaking, we plot the functions, i.e., F_1 and F_2, versus ω and r as shown in Fig. 9. They form two curved surfaces in the three-dimensional space. The zero-plane (yellow) is also plotted. It is easy to know that the solutions must exist on the zero-plane. In addition, the solutions must be on the intersection edge of the curved surface F_1 and the curved surface F_2. Fig. 9**(a)** shows the result when $\theta = 190$ μN/V. In Fig. 9**(a)**, we find no intersection of the two curved surfaces, which implies that there is no solution to Eqs. (50) and (51). As predicted by the impedance matching theory, when the electromechanical coupling strength is weak, the power limit cannot be attained. The result in Fig. 9**(a)** tallies with the impedance matching theory.

Subsequently, θ is then increased to 1900 μN/V. Fig. 9**(b)** shows the corresponding results. Two intersection points are observed in Fig. 9**(b)**, which indicate two solutions to Eqs. (50) and (51). According to the theory in Section 5 and the conclusions in [42,44], the existence of two solutions indicates that θ = 1900 μN/V corresponds to a strong coupling case. By substituting the graphically identified solutions into Eq. (49), the power limit of the SDOF PEH under combined excitations is estimated to be about 70.09 mW. We also numerically compute the maximum power output from the SDOF PEH by sweeping the resistance for verification. The results are presented in Fig. 10. It can be seen that when θ is small, the maximum power amplitude is quite small. When θ is increased to a certain level, e.g., $\theta = 5 \times 190$ μN/V which represents a nearly critically coupled case, the maximum power amplitude approaches a constant value.

Further increasing θ to 1900 μN/V cannot increase the power amplitude anymore. But it is noted that when $\theta = 1900$ μN/V, there appear two peaks in the power spectrum. The appearance of dual-peaks in the power spectrum agrees with the double-solution case shown in Fig. 9**(b)**. The phenomena revealed by the numerical results seem to be able to capture the characteristics SDOF PEH on power limit, conforming to the above power limit analysis. Unfortunately, the maximum power amplitude does not match the above theory: the actual power limit identified from the numerical results is about 94.78 mW, which is much larger than the predicted power limit (i.e., 70.09 mW) using the impedance matching theory.

To address the concern of any mathematical mistakes in the above theory, we employ it to investigate a classical linear PEH as an additional verification. To be more specific, we let s_1 and s_3 be zero to neglect the aerodynamic force effect. As the strong coupling case is of the most interest, θ is set to be 1900 μN/V. Fig. 11 presents the power spectrum and the impedance plot of the SDOF PEH without the influence of the aerodynamic force. The power spectrum in Fig. 11**(a)** is obtained by numerically sweeping the resistance. The power limit is evaluated using Eq. (49). Both results show that the power limit of the linear case is about 208.9 mW. It can be found that

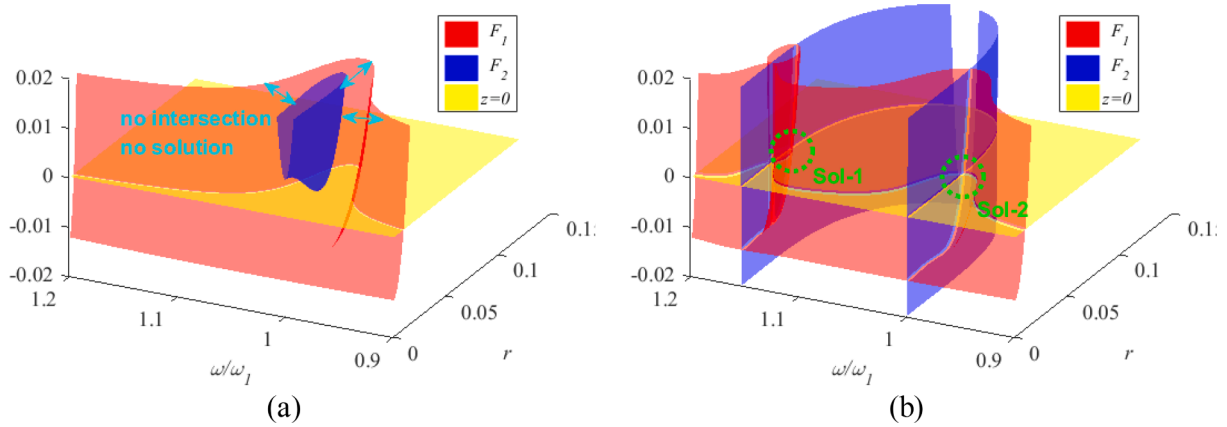

Fig. 9. F_1 and F_2 versus ω and r (a) when $\theta = 190$ μN/V, (b) when $\theta = 1900$ μN/V.

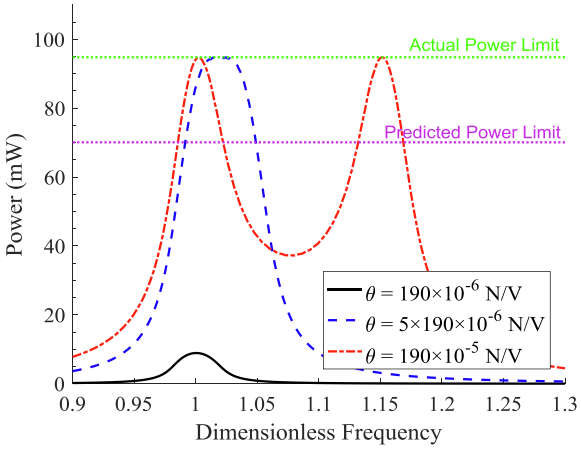

Fig. 10. Maximum power of the SDOF PEH with different electromechanical coupling strength.

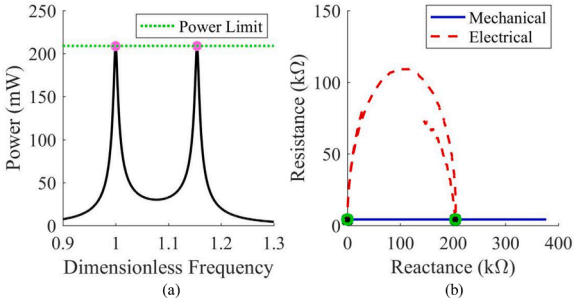

Fig. 11. (a) Power spectrum of the SDOF PEH without the influence of the aerodynamic force when $\theta = 1900$ μN/V; (b) the corresponding impedance plot. The green circles and black crosses in the right-column graph, respectively, indicate the corresponding mechanical and electrical impedances of the power limit cases marked with purple points in the left-column graph. Note that the black crosses overlap with the green circles. (For interpretation of the references to colour in this figure legend, the reader is referred to the web version of this article.)

for the linear case, the impedance matching theory well predicts the power limit of the SDOF PEH. Fig. 11**(b)** shows the corresponding impedance plot based on the numerical results. It is observed that when the power limit is achieved, the mechanical impedance (internal impedance) matches the electrical impedance (external impedance). Thus, the results in Fig. 11**(b)** further confirm the impedance matching theory. In addition, we can note that the impedance matching occurs at two places, which explains the dual-peaks phenomenon in Fig. 11**(a)**.

From the above studies, it is noted that the power limit derived based on the impedance matching theory is applicable for the linear case but not the nonlinear case. We thus speculate that impedance matching may not be the essential condition for attaining the power limit of the SDOF PEH under the combined excitations. To answer this question, the impedance plots of the SDOF PEH under the combined excitations are examined. Fig. 12 shows the results of the SDOF PEH with different electromechanical coupling strengths. Note that 'Mechanical' and 'Electrical' in the legend denote the mechanical (internal) and electrical (external) impedances, respectively. Fig. 12**(a) and (b)** present the results of a weakly coupled case (i.e., $\theta = 190$ μN/V). The maximum power attained is only about 8.913 mW. By inspecting the impedance plot, it can be seen that there is no intersection of the mechanical and electrical impedance curves. This agrees with the theory in Section 5 that when the electromechanical coupling strength is small (i.e., Eq. (48)), the impedance matching condition can not be satisfied.

Figure 12**(c) and (d)** present the results of the case close to critical coupling strength (i.e., $\theta = 5 \times 190$ μN/V). According to the impedance matching theory, a critically coupled case should have a single solution. The results in Fig. 12**(c)** are obtained by numerically sweeping the resistance. Since the sweeping rate cannot be infinitely small, the numerical results exhibit minor ripples around the peak. For this reason, we pick several points with almost the same amplitudes on top of the peak in the power spectrum to find their corresponding impedances. From Fig. 12**(d)**, it is observed that the electrical and mechanical impedances have one intersection point. However, the power limit is not attained at this intersection point, i.e., the impedance matching condition. Instead, the power limit is achieved when the mechanical and electrical impedance are, respectively, at the green circles and black crosses in the impedance plot. The result in Fig. 12**(d)** preliminarily suggests that the power limit of the SDOF PEH under the combined excitations does not follow the impedance matching theory.

The results for a strong coupling strength (i.e., $\theta = 1900$ μN/V) are presented in Fig. 12**(e) and (f)**. As compared with the critically coupled case, the maximum power attained is almost the same, around 94.78 mW. Fig. 12**(f)** is the counterpart of Fig. 11**(b)**. It can be

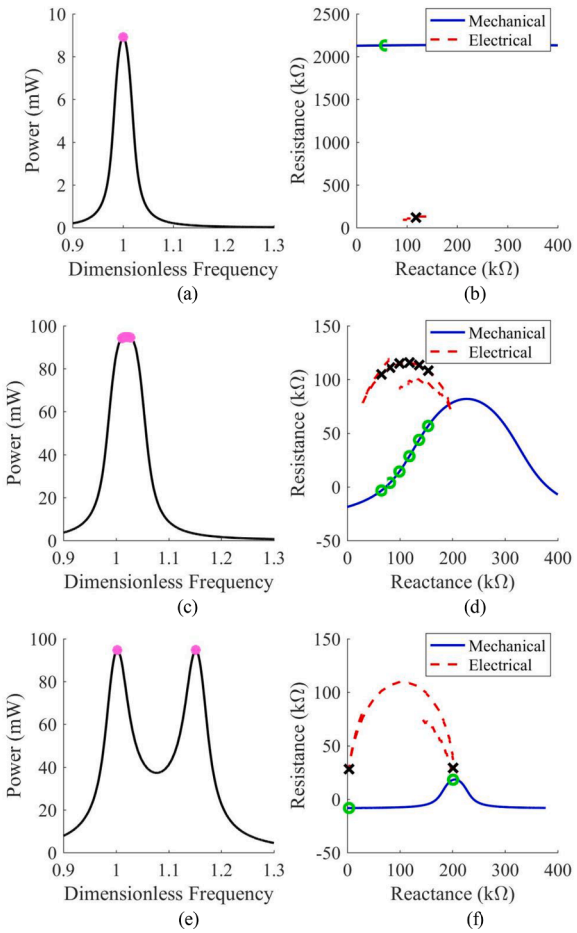

Fig. 12. Power spectrum of SDOF PEH under combined excitations for (a) $\theta = 190$ μN/V, (c) $\theta = 5 \times 190$ μN/V, (e) $\theta = 1900$ μN/V; and corresponding impedance plots for (b) $\theta = 190$ μN/V, (d) $\theta = 5 \times 190$ μN/V, (f) $\theta = 1900$ μN/V. The green circles and black crosses in the right-column graphs, respectively, indicate the corresponding mechanical and electrical impedances of the power limit cases marked with purple points in the left-column graphs. (For interpretation of the references to colour in this figure legend, the reader is referred to the web version of this article.)

found that for the linear case (Fig. 11**(b)**), the power limit is attained when the mechanical and electrical impedances match each other. However, the results in Fig. 12**(f)** clearly indicate that it is not the case for the SDOF PEH under the combined excitations, where the power limit is achieved when the mechanical and electrical impedance are, respectively, at the green circles and black crosses. These results further confirm that the impedance matching theory becomes invalid for analysing the power limit of the SDOF PEH under the combined excitations. The potential reason for the inapplicability of the impedance theory is provided below. In the linear PEHs, the impedance theory is applicable, since the internal resistance (i.e., the damping coefficient in the mechanical domain) is invariant [42]. Hence, impedance matching is the only condition to obtain the maximum power output. For the nonlinear PEH investigated in Lan et al. [44], nonlinearity exists as a stiffness term, and the damping coefficient is still invariant. Therefore, the impedance theory can be extended to analyse the power limit of that nonlinear PEH. Unfortunately, the SDOF PEH presented in this study involves a nonlinearity in the form of a damping-like term in the governing equations. Thus, the internal resistance of the SDOF PEH under the combined excitations is variant. To explain that the impedance matching theory is not applicable for the case with a variant internal resistance, we provide a simple but straightforward mathematical proof below.

First, the maximum power transfer theorem is briefly reviewed. Considering a general voltage source shunted to a resistance load, the power transferred from the source to the load resistor can be written as:

$$P = \frac{V_{sourece}^2 R_{external}}{(R_{internal} + R_{external})^2} \tag{52}$$

Assuming the internal resistance, i.e., $R_{internal}$, is a constant, taking the derivative of P to $R_{external}$, then forcing it to be zero, one obtains the solution of the optimal resistance for obtaining the maximum power. By following the above procedures, it is found as in Eq. (53) that the maximum power that can be transferred from the source to the load when the internal resistance exactly matches the load resistance.

$$\frac{\partial P}{\partial R_{external}} = \frac{V_{source}^2 (R_{internal} - R_{external})}{(R_{internal} + R_{external})^3} = 0 \tag{53}$$

The above statement is the maximum power transfer theorem. As discussed in Section 5, for the SDOF PEH under the combined excitations, its internal resistance is both frequency and amplitude-dependent. Note that the dynamic response amplitude is actually dependent on the load resistance, especially under the strong coupling condition. Therefore, the internal resistance is, in fact, dependent on the external resistance. Taking the derivative of P to $R_{external}$, then forcing it to be zero yields:

$$\frac{\partial P}{\partial R_{external}} = \frac{V_{source}^2 \left(-2R_{external} \frac{\partial R_{internal}}{\partial R_{external}} + R_{internal} - R_{external} \right)}{(R_{external} + R_{internal})^3} = 0 \tag{54}$$

According to Eq. (54), it can be found that as $\frac{\partial R_{internal}}{\partial R_{external}} \neq 0$, the maximum power transfer is not realized at $R_{internal} = R_{external}$. Note that in the above derivations, the reactance components are neglected just for simplicity. The above conclusion is still valid even the reactance components are taken into account.

Prior to the concluding remarks, one may notice that all the above results are obtained based on the simplified model (i.e., Eqs. (37) and (38)) presented in Section 5. Whether these predictions are valid for the original model (i.e., Eqs. (1) and (2)) remains a question that has not been answered. To answer the question, we substitute the optimal parameters predicted based on the simplified model into the original model (i.e., Eqs. (1) and (2)) for simulation. The system parameters are the same as those listed in Table 1, a strong coupling coefficient $\theta = 1900$ μN/V is used to enable the attainability of the power limit. Both the actual optimal parameters obtained using resistance sweeping and the predicted optimal parameters determined using the impedance matching theory are listed in Table 2.

The simulation results based on the original model are presented in Fig. 13. The base excitation frequency and the load resistance are set according to the parameters given in Table 2. Using the optimal parameters obtained based on resistance sweeping, the results in Fig. 13**(a) and (b)** correspond to the first and second power peaks, respectively, where the voltage amplitudes are 51.89 and 366.30 V, respectively. Using the optimal parameters obtained based on the impedance matching theory, Fig. 13**(c) and (d)** show the voltage responses corresponding to the first and second power peaks, respectively, with amplitudes of 29.87 V and 480.40 V, respectively. As compared to the results in Table 2, it can be found that the results from the numerical simulations based on the original model are in good agreement with the results obtained based on the simplified model. Therefore, the power limit analysis presented in this section is thus well verified.

7. Conclusions

This paper has presented a rigorous solution to the dynamic response of an SDOF PEH under the combined wind and base excitations. The boundaries of quenching have also been derived for providing an in-depth understanding of the dynamics of the SDOF PEH under the combined excitations. According to electrical–mechanical analogies, an equivalent circuit model has been developed with consideration of the base excitation and the aerodynamic force induced by the wind load. The equivalent circuit simulation results have verified the analytical solutions in terms of both the voltage frequency response and the boundaries of quenching. Moreover, the power limit analysis of the SDOF PEH has been explored for the first time. The impedance matching theory has been first employed to predict the power limit of the SDOF PEH under the combined excitations, and the expression of the power limit has been derived. In addition, the maximum power amplitudes have been sought by sweeping the resistance. The comparison results, together with the impedance plots, have indicated that impedance matching is not the condition of attaining the power limit of the SDOF PEH under the combined excitations. A simple yet straightforward proof has been offered to explain the inapplicability of the impedance matching theory in the present case. In brief, due to the damping-like aerodynamic force, the total effective damping in the mechanical domain becomes a function of the load resistance. Therefore, the equivalent internal resistance becomes variant, and the classic maximum power transfer theorem is no longer valid. The methodologies and conclusions presented in this paper can provide some guidelines for analysing similar piezoelectric energy harvesting systems in the future.

Table 2
The optimal parameters obtained based on the simplified model.

	Actual (resistance sweeping)	Predicted (impedance matching)
First peak	$\omega/\omega_1 = 1.0024$ $V_{op} = 51.93$ V $R_{op} = 2.848 \times 10^4$ Ω $P_{lim} = 94.78$ mW	$\omega/\omega_1 = 1.0005$ $V_{op} = 29.89$ V $R_{op} = 1.274 \times 10^4$ Ω $P_{lim} = 70.1$ mW
Second peak	$\omega/\omega_1 = 1.1515$ $V_{op} = 366.53$ V $R_{op} = 1.417 \times 10^4$ Ω $P_{lim} = 94.80$ mW	$\omega/\omega_1 = 1.1539$ $V_{op} = 480.29$ V $R_{op} = 3.291 \times 10^4$ Ω $P_{lim} = 70.1$ mW

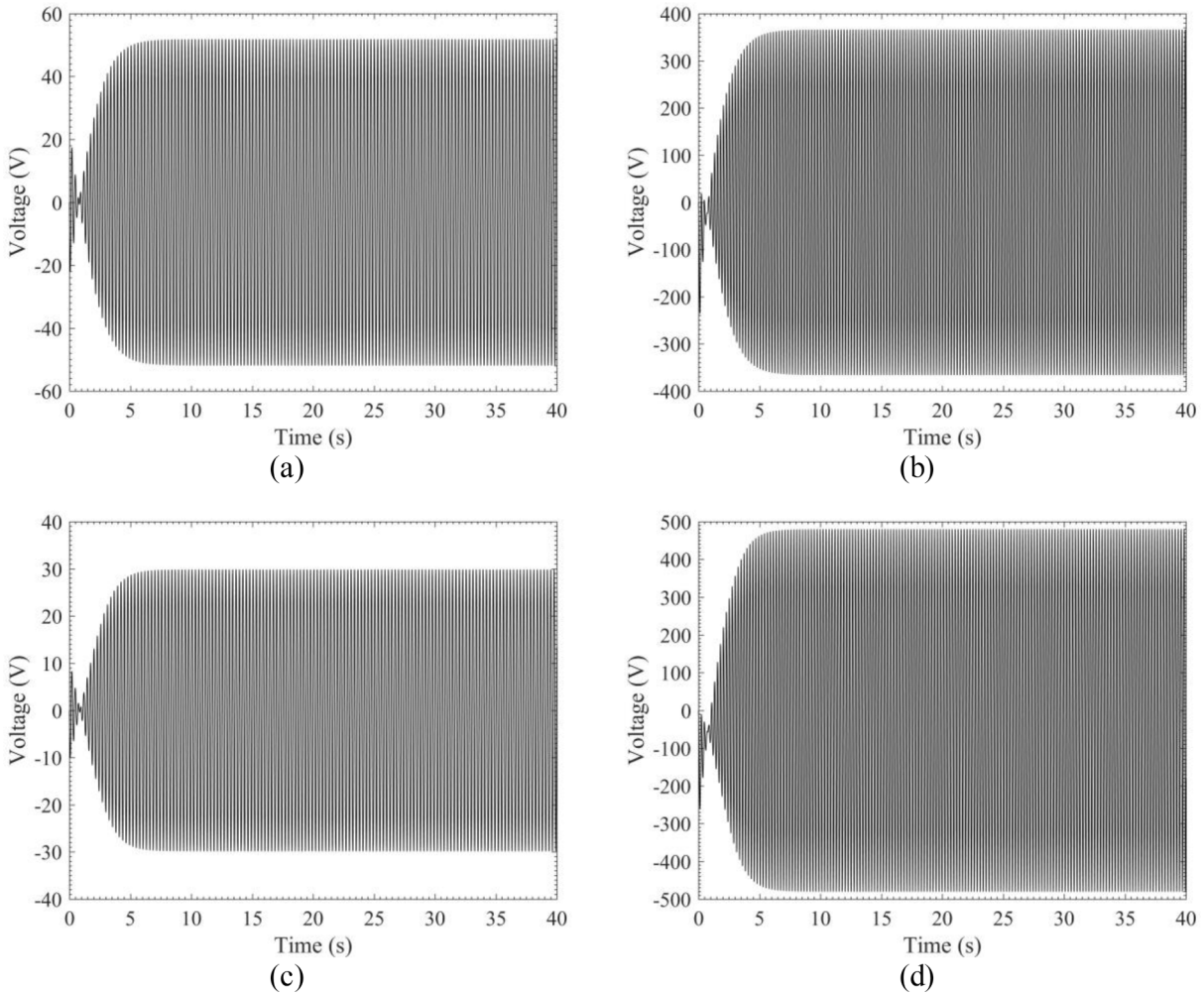

Fig. 13. The time-history voltage responses of the SDOF PEH under the combined excitations: (a) $\omega/\omega_1 = 1.0024$, $R_{op} = 2.848 \times 10^4$ Ω; (b) $\omega/\omega_1 = 1.1515$, $R_{op} = 1.417 \times 10^4$ Ω; (c) $\omega/\omega_1 = 1.0005$, $R_{op} = 1.274 \times 10^4$ Ω; (d) $\omega/\omega_1 = 1.1539$, $R_{op} = 3.291 \times 10^4$ Ω.

Declaration of Competing Interest

The authors declare that they have no known competing financial interests or personal relationships that could have appeared to influence the work reported in this paper.

Acknowledgement

This work was financially supported by the State Key Laboratory of Structural Analysis for Industrial Equipment, Dalian University of Technology, China (GZ21114).

References

[1] H.A. Sodano, D.J. Inman, G. Park, A review of power harvesting from vibration using piezoelectric materials, Shock Vib. Digest 36 (3) (2004) 197–206.
[2] S. Priya, D.J. Inman, Energy Harvesting Technologies, Vol. 21, Springer, New York, 2009.
[3] L. Tang, Y. Yang, C.K. Soh, Toward broadband vibration-based energy harvesting, J. Intell. Mater. Syst. Struct. 21 (18) (2010) 1867–1897.
[4] C.A. Howells, Piezoelectric energy harvesting, Energy Convers. Manage. 50 (7) (2009) 1847–1850.
[5] S. Fang, X. Fu, X. Du, W.-H. Liao, A music-box-like extended rotational plucking energy harvester with multiple piezoelectric cantilevers, Appl. Phys. Lett. 114 (23) (2019), 233902.
[6] G. Hu, L. Tang, J. Liang, C. Lan, R. Das, Acoustic-elastic metamaterials and phononic crystals for energy harvesting: a review, Smart Mater. Struct. 30 (8) (2021), 085025.
[7] W. Shen, S. Zhu, H. Zhu, Unify energy harvesting and vibration control functions in randomly excited structures with electromagnetic devices, J. Eng. Mech. 145 (1) (2019) 04018115.
[8] W. Shen, Z. Long, H. Wang, H. Zhu, Power analysis of SDOF structures with tuned inerter dampers subjected to earthquake ground motions, ASCE-ASME J. Risk Uncertainty Eng. Syst., Part B: Mech. Eng. 7 (1) (2021), 010907.

[9] J. Wang, L. Tang, L. Zhao, G. Hu, R. Song, K. Xu, Equivalent circuit representation of a vortex-induced vibration-based energy harvester using a semi-empirical lumped parameter approach, Int. J. Energy Res. 44 (6) (2020) 4516–4528.
[10] J. Wang, G. Hu, Z. Su, G. Li, W. Zhao, L. Tang, L. Zhao, A cross-coupled dual-beam for multi-directional energy harvesting from vortex induced vibrations, Smart Mater. Struct. 28 (12) (2019) p. 12LT02.
[11] C. Lan, L. Tang, G. Hu, W. Qin, Dynamics and performance of a two degree-of-freedom galloping-based piezoelectric energy harvester, Smart Mater. Struct. 28 (4) (2019), 045018.
[12] G. Hu, J. Liang, L. Tang, J. Wang, Improved theoretical analysis and design guidelines of a two-degree-of-freedom galloping piezoelectric energy harvester, J. Intell. Mater. Syst. Struct. (2021), p. 1045389X211011681.
[13] H. Liu, X. Gao, Vibration energy harvesting under concurrent base and flow excitations with internal resonance, Nonlinear Dyn. 96 (2) (2019) 1067–1081.
[14] M. Eugeni, H. Elahi, F. Fune, L. Lampani, F. Mastroddi, G.P. Romano, P. Gaudenzi, Numerical and experimental investigation of piezoelectric energy harvester based on flag-flutter, Aerosp. Sci. Technol. 97 (2020), 105634.
[15] K. Shoele, R. Mittal, Energy harvesting by flow-induced flutter in a simple model of an inverted piezoelectric flag, J. Fluid Mech. 790 (2016) 582–606.
[16] Y. Yang, L. Zhao, L. Tang, Comparative study of tip cross-sections for efficient galloping energy harvesting, Appl. Phys. Lett. 102 (6) (2013), 064105.
[17] A. Barrero-Gil, D. Vicente-Ludlam, D. Gutierrez, F. Sastre, Enhance of energy harvesting from transverse galloping by actively rotating the galloping body, Energies 13 (1) (2020) 91.
[18] A. Barrero-Gil, G. Alonso, A. Sanz-Andres, Energy harvesting from transverse galloping, J. Sound Vib. 329 (14) (2010) 2873–2883.
[19] A. Bibo, A.H. Alhadidi, M.F. Daqaq, Exploiting a nonlinear restoring force to improve the performance of flow energy harvesters, J. Appl. Phys. 117 (4) (2015), 045103.
[20] J. Wang, L. Geng, S. Zhou, Z. Zhang, Z. Lai, D. Yurchenko, Design, modeling and experiments of broadband tristable galloping piezoelectric energy harvester, Acta Mech. Sin. (2020) 1–14.
[21] L. Zhao, Y. Yang, An impact-based broadband aeroelastic energy harvester for concurrent wind and base vibration energy harvesting, Appl. Energy 212 (2018) 233–243.
[22] C. Lan, G. Hu, W. Qin, Y. Liao, A wind-induced negative damping method to achieve high-energy orbit of a nonlinear vibration energy harvester, Smart Mater. Struct. 30 (2021) p. 02LT02.
[23] H.L. Dai, A. Abdelkefi, U. Javed, L. Wang, Modeling and performance of electromagnetic energy harvesting from galloping oscillations, Smart Mater. Struct. 24 (4) (2015), 045012.
[24] G. Hu, J. Wang, H. Qiao, L. Zhao, Z. Li, L. Tang, An experimental study of a two-degree-of-freedom galloping energy harvester, Int. J. Energy Res. 45 (2) (2021) 3365–3374.
[25] G. Hu, J. Wang, L. Tang, A comb-like beam based piezoelectric system for galloping energy harvesting, Mech. Syst. Sig. Process. 150 (2021), 107301.
[26] A. Bibo, M.F. Daqaq, Energy harvesting under combined aerodynamic and base excitations, J. Sound Vib. 332 (20) (2013) 5086–5102.
[27] A. Bibo, M. Daqaq, Investigation of concurrent energy harvesting from ambient vibrations and wind using a single piezoelectric generator, Appl. Phys. Lett. 102 (24) (2013), 243904.
[28] H. Dai, A. Abdelkefi, L. Wang, Piezoelectric energy harvesting from concurrent vortex-induced vibrations and base excitations, Nonlinear Dyn. 77 (3) (2014) 967–981.
[29] Z. Yan, A. Abdelkefi, M.R. Hajj, Piezoelectric energy harvesting from hybrid vibrations, Smart Mater. Struct. 23 (2) (2014), 025026.
[30] A. Bibo, A. Abdelkefi, M.F. Daqaq, Modeling and characterization of a piezoelectric energy harvester under combined aerodynamic and base excitations, J. Vib. Acoust. 137 (3) (2015).
[31] Z. Yan, H. Lei, T. Tan, W. Sun, W. Huang, Nonlinear analysis for dual-frequency concurrent energy harvesting, Mech. Syst. Sig. Process. 104 (2018) 514–535.
[32] L. Zhao. Analytical solutions for a broadband concurrent aeroelastic and base vibratory energy harvester. in Active and Passive Smart Structures and Integrated Systems XII. 2019. International Society for Optics and Photonics.
[33] E. Lefeuvre, A. Badel, C. Richard, D. Guyomar, Piezoelectric energy harvesting device optimization by synchronous electric charge extraction, J. Intell. Mater. Syst. Struct. 16 (10) (2005) 865–876.
[34] M. Lallart, L. Garbuio, L. Petit, C. Richard, D. Guyomar, Double synchronized switch harvesting (DSSH): a new energy harvesting scheme for efficient energy extraction, IEEE Trans. Ultrason. Ferroelectr. Freq. Control 55 (10) (2008) 2119–3000.
[35] D. Guyomar, A. Badel, E. Lefeuvre, C. Richard, Toward energy harvesting using active materials and conversion improvement by nonlinear processing, IEEE Trans. Ultrason. Ferroelectr. Freq. Control 52 (4) (2005) 584–595.
[36] Y.C. Shu, I.C. Lien, Analysis of power output for piezoelectric energy harvesting systems, Smart Mater. Struct. 15 (6) (2006) 1499–1512.
[37] M. Lallart, G. Lombardi, Synchronized switch harvesting on ElectroMagnetic system: a nonlinear technique for hybrid energy harvesting based on active inductance, Energy Convers. Manage. 203 (2020), 112135.
[38] M. Lallart, Nonlinear technique and self-powered circuit for efficient piezoelectric energy harvesting under unloaded cases, Energy Convers. Manage. 133 (2017) 444–457.
[39] H. Abdelmoula, A. Abdelkefi, The potential of electrical impedance on the performance of galloping systems for energy harvesting and control applications, J. Sound Vib. 370 (2016) 191–208.
[40] L. Zhao, Y. Yang, Analytical solutions for galloping-based piezoelectric energy harvesters with various interfacing circuits, Smart Mater. Struct. 24 (7) (2015), 075023.
[41] L. Zhao, Y. Yang, Comparison of four electrical interfacing circuits in wind energy harvesting, Sens. Actuators, A 261 (2017) 117–129.
[42] Y. Liao, H. Sodano, Optimal power, power limit and damping of vibration based piezoelectric power harvesters, Smart Mater. Struct. 27 (7) (2018), 075057.
[43] Y. Liao, J. Liang, Unified modeling, analysis and comparison of piezoelectric vibration energy harvesters, Mech. Syst. Sig. Process. 123 (2019) 403–425.
[44] C. Lan, Y. Liao, G. Hu, L. Tang, Equivalent impedance and power analysis of monostable piezoelectric energy harvesters, J. Intell. Mater. Syst. Struct. 31 (14) (2020) 1697–1715.
[45] Y. Yang, L. Tang, Equivalent circuit modeling of piezoelectric energy harvesters, J. Intell. Mater. Syst. Struct. 20 (18) (2009) 2223–2235.